
Unsupervised Video Prediction from a Single Frame by Estimating 3D Dynamic Scene Structure

Paul Henderson
paul@pmh47.net

Christoph H. Lampert *
chl@ist.ac.at

Bernd Bickel *
bernd.bickel@ist.ac.at

Institute of Science and Technology (IST) Austria

<http://pmh47.net/vipl4s/>

Abstract

Our goal in this work is to generate realistic videos given just one initial frame as input. Existing unsupervised approaches to this task do not consider the fact that a video typically shows a 3D environment, and that this should remain coherent from frame to frame even as the camera and objects move. We address this by developing a model that first estimates the latent 3D structure of the scene, including the segmentation of any moving objects. It then predicts future frames by simulating the object and camera dynamics, and rendering the resulting views. Importantly, it is trained end-to-end using only the unsupervised objective of predicting future frames, without any 3D information nor segmentation annotations. Experiments on two challenging datasets of natural videos show that our model can estimate 3D structure and motion segmentation from a single frame, and hence generate plausible and varied predictions.

1 Introduction

Predicting the future from a single image is a compelling problem. As humans, we can readily imagine what might happen next in the scenario depicted in an image—which objects are moving, which are static, where the camera might move to. Indeed, we can visualize different possible futures, e.g. with a particular car being either parked or driving, when this is uncertain given just a single image. However, this task remains challenging for machine learning methods, as the predicted video is very high-dimensional, yet must retain temporal coherence over a number of frames.

Most real-world videos are filmed by a camera moving through a dynamic 3D environment or *4D scene*. This scene is typically stable, in the sense that many aspects remain constant—for example, the shape of a car or the color of a dog do not change over time, even though the car, dog and camera may be moving. State-of-the-art unsupervised methods for future prediction cannot exploit this powerful prior knowledge. They rely on black-box generative models [8, 13, 23], that must instead try to learn it from data. In practice, they often fail to do so, with objects slowly changing in shape or texture over time [46].

We propose a novel approach to video prediction from a single frame, that first estimates the 3D structure of the scene depicted in that frame—its 3D geometry, texture, and segmentation into moving entities (Section 2). We assume that the camera and other entities in the scene move, but retain their original appearance and geometry; this allows us to generate future frames by predicting their motion, and re-rendering the updated scene. Of course, learning to predict 3D structure and motion segmentation from a single image is a challenging problem in itself, with state-of-the-art methods

*Equal advising

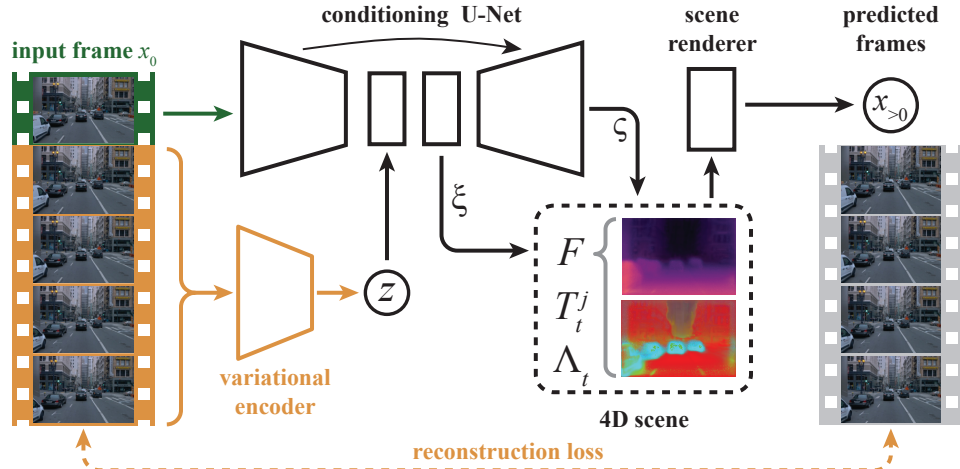


Figure 1: Overview of our conditional generative model of video. Given a single frame x_0 , our model learns to generate plausible video clips $x_{>0}$. We decode x_0 and a latent Gaussian embedding z to give a 4D scene, consisting of the 3D structure and motion segmentation (represented by a function F), camera motion Λ_t , and transformations of moving entities T_t^j . Our method is trained like a VAE (orange) to reconstruct input frames via z and the 3D scene representation.

relying on extensive supervision [35, 27, 15]. Here we adopt an entirely *unsupervised* approach, that requires only monocular RGB videos during training. **Our model is trained end-to-end for video prediction, treating the 4D scene structure as a latent factor to be estimated.** We adopt a variational approach that handles the inherent stochasticity of the problem, and is able to sample different possible structures and future motion for a given frame.

As a key ingredient in our model, we develop a novel representation of 4D scenes, that factors geometry and motion information. We build on the static scene representation of [30], modifying it to represent the segmentation of a scene into comoving regions. This allows us to use a low-dimensional, factorized motion representation, specifying time-varying transforms for each of a small number of motion components, rather than a dense flow field for the entire scene. It also directly captures the prior knowledge that many points in a scene typically move together (e.g. all the points within an object), without the need for extra regularization.

We conduct a comprehensive evaluation of our method on two datasets of challenging real-world videos (Section 4). Unlike most datasets used in prior works [8, 24, 13], these include (unknown) 3D camera motion and complex appearances. We show that our method successfully recovers scene structure, and can use this to generate diverse and plausible predictions of future frames. Moreover, its quantitative performance significantly exceeds an existing state-of-the-art work [13].

Contributions. In summary, our contributions are as follows:

- we propose a novel representation for multi-object 4D scenes
- we show how to incorporate this in a conditional generative model of videos, that can be trained without supervision
- ours is the first unsupervised video prediction method that ensures predicted frames represent a coherent 4D scene

2 Method

We cast the problem of stochastic video prediction as drawing samples from a conditional generative model (Figure 1). We use x_0 to denote the initial frame that is provided as conditioning. To define the conditional distribution $P(x_1, \dots, x_L | x_0)$ on L subsequent frames $(x_1, \dots, x_L) \equiv x_{>0}$, we introduce a latent variable z that will capture all uncertainty about the future, i.e. embed all information that is not present in x_0 . This will include the camera and object motion, and the appearance of regions disoccluded by moving objects. This leads to a probabilistic model of the

form $P(x_{>0} | x_0) = P(z) P(x_{>0} | z, x_0)$. As is common [21, 38], we choose z to be a multivariate standard Gaussian distribution, i.e. $z \sim \mathcal{N}(\mathbf{0}, I)$. To ensure the generated clip depicts a consistent scene, the conditional distribution on future frames $P(x_{>0} | z, x_0)$ is given by first mapping x_0 and z to a description \mathcal{S} of a 4D scene, incorporating geometry, texture, segmentation, and motion (dashed box in Figure 1). Then, the frames x_t for $t > 0$ are generated by *rendering* \mathcal{S} at the relevant times t , and finally adding Gaussian pixel noise to ensure the data likelihood is always defined. Note the contrast with earlier works [8, 24, 13] that predict $x_{>0}$ directly from x_0 and z , e.g. using a CNN, and without the intermediate representation \mathcal{S} that ensures a consistent scene is shown.

We first describe a recently-proposed static scene representation [30] and how it is rendered to pixels; we then extend it to give our 4D scene representation \mathcal{S} . Next, we discuss how our representation is conditioned on x_0 and z , to allow inferring it from a single frame and incorporating it into our probabilistic model. Finally, we describe how the overall model is trained end-to-end.

Background: NeRF representation of static scenes. *Neural radiance fields* (NeRFs) [30] represent a single static scene using a function F that maps points $p \in \mathbb{R}^3$ in the 3D space of the scene to a density ρ and an RGB color $c \in [0, 1]^3$. The density $\rho \in \mathbb{R}^+$ represents the differential probability that a light ray cast from the camera will terminate (i.e. hit some matter) at point p ; zero corresponds to free space, and large values to solid objects. In practice F is a densely-connected neural network, with p preprocessed using the Fourier embedding method of [43]. To render the scene defined by F , standard quadrature-based volume rendering techniques [29, 30, 28], are used. Specifically, to calculate the color $C(q)$ of the pixel at coordinate q , we evaluate F at K points along the ray cast from q into the scene through the camera lens, setting

$$C(q) = \sum_{k=1}^K V_k (1 - \exp(-\rho(r_k)\delta_k)) c(r_k), \quad \text{where } V_k = \exp\left(-\sum_{k'=1}^{k-1} \rho(r_{k'})\delta_{k'}\right) \quad (1)$$

Here r_k gives the k^{th} 3D sample point along the ray from q , and $\delta_k = \|r_{k+1} - r_k\|$ is the spacing between samples. Intuitively, V_k represents how visible the k^{th} sample is in spite of occlusion by nearer samples.

Our 4D scene representation. We represent a 4D scene \mathcal{S} as three parts: (i) the static scene geometry and appearance at $t = 0$; (ii) its segmentation into J different *motion components*; and (iii) a set of time-varying transformations $T_t^{1 \dots J}$ capturing these components’ motion for $t > 0$. Intuitively, each motion component is a region of 3D space in the scene, in which all the points are moving coherently. The model is free to use motion components to represent individual moving objects (e.g. a car), comoving groups of objects (e.g. a convoy of cars), or the static background. The transformation T_t^j defines how points in the initial scene belonging to component j are mapped to their location in frame t . To implement this, we introduce a *scene function*, $F(p) = [\rho(p), c(p), \omega(p)]$; here ρ and c are the density and color at point p in the 3D scene corresponding to $t = 0$, similar to above. In order to capture the fact that different regions of the scene belong to different motion components, F also outputs a vector $\omega \in [0, 1]^J$ of values indicating which of J components each point belongs to; these are normalized by a softmax. Intuitively, if ω is one-hot with $\omega_j(p) = 1$, then the point p will transform according to T_t^j ; if ω is not one-hot, then corresponding fractions of the density at p will transform according to each T_t^j .

Together, the scene function F and component transformations $T_t^{1 \dots J}$ define the distribution of density and color in all frames $t = 1 \dots L$. To render frame t , we adapt (1) to our dynamic multiple-component setting. Suppose that the camera transformation (i.e. extrinsic matrix, representing its location and rotation) in frame t is denoted by Λ_t . We calculate the density and color for point p at time t by applying the inverse of the component transformations, to find which location p_0^j in the initial scene would be transported to p by the j^{th} component’s motion, i.e. $p_0^j = (T_t^j)^{-1}[p]$. Compared with (1), we must now evaluate F once per motion component for each sample; this effectively defines one opacity per component, and we weight these according to ω_j , before summing to give the combined density and color. Therefore, the expected color $x_t(q)$ of the pixel at coordinate q in predicted frame x_t is given by

$$x_t(q) = \sum_{k=1}^K \left\{ V_k \sum_{j=1}^J \left[\alpha_k^j \omega_j ((T_t^j)^{-1}[r_k^t]) c((T_t^j)^{-1}[r_k^t]) \right] \right\} \quad (2)$$

where

$$V_k = \exp \left(\sum_{k'=1}^{k-1} \log \prod_{j=1}^J (1 - \alpha_k^j) \omega_j ((T_t^j)^{-1} [r_{k'}^t]) \delta_{k'} \right) \quad (3)$$

and

$$\alpha_k^j = 1 - \exp \left(- \rho ((T_t^j)^{-1} [r_k^t]) \delta_k \right) \quad (4)$$

Here r_k^t gives the k^{th} 3D sample point along the ray cast from the camera at pixel q of frame t ; this has an implied dependence on the camera transformation Λ_t . Note that ω weights the sample opacities α_k^j , (i.e. is applied *after* integrating the densities) as these lie in $[0, 1]$. Although more intuitive, directly weighting the density ρ has no practical effect, as ρ is unbounded hence arbitrarily-large density may be assigned to all components, rather than the desired outcome of ω ‘splitting’ a finite density between components.

Conditioning the scene representation. The scene function F and transformations $T_t^{1 \dots J}$ and Λ_t corresponding to a given input frame x_0 must be inferred from that frame and the latent z . We therefore introduce a U-Net [39] *conditioning network*², that has x_0 as input, and injects z as conditioning at the bottleneck layer; from this we extract a 2D feature map ζ and an embedding vector ξ .

ξ is decoded by a densely-connected network to give parameters of the transformations $T_t^{1 \dots J}$ and Λ_t for the components and camera respectively. We experiment with two different parametrizations of Λ_t : (i) a general model that allows arbitrary camera translation and yaw/pitch; (ii) a vehicle-specific model that captures the prior knowledge that cameras mounted on cars are typically restricted to motion parallel with the ground plane, characterized by a forward speed and azimuthal velocity. We hypothesize this additional prior knowledge will make the learning task easier, as the model does not have to waste representational capacity learning it. The precise specifications of these parametrizations are given in Appendix B.

The conditioning variables ζ and ξ also influence the scene function F in two ways. First, ξ is used as input to FiLM conditioning layers [32] following each hidden-layer activation³. Second, when evaluating F at a 3D location p at time t , we map p back into the 3D space of the initial frame ($t = 0$) by applying the inverse of the predicted camera transformation and each of the component transformations at time t . Then, we bilinearly sample the feature map ζ , and provide these features as an additional input to F , concatenated with p , similar to [49].

Training and regularization. We have now specified the full conditional generative model $P(x_{>0} | x_0)$. To train this model, we would ideally maximize the likelihood of future frames given initial frames. However, this is intractable as we must marginalize the latent variable z ; we therefore use Stochastic Gradient Variational Bayes [21, 38]. Specifically, we introduce a variational posterior distribution $Q(z | x_0, x_{>0})$, chosen to be a diagonal Gaussian. Its mean and log-variance are predicted by an encoder network $\text{enc}_\phi(x_0, x_{>0})$. For this we use a 3D CNN taking the concatenated frames as input (orange components in Figure 1). Intuitively, as the encoder has access to complete video clips at training time, it should learn to embed information about motion and disoccluded regions in z , so the decoder can learn to reconstruct them. In practice, the model is trained end-to-end to maximize the evidence lower bound (ELBO) [21, 38] using Adam [20]; as in [17], we multiply the KL-divergence term by a weight β , which is linearly increased from zero during the start of training. We also add a reconstruction loss for x_0 , with the component and camera transformations set to the identity.

To reduce computational intensity, we only reconstruct a sparse subset of points q in each frame. Moreover, to reduce the number of samples K required along each ray, we also pretrain the unsupervised single-frame depth-prediction method of [25] on our data, and use this to guide the sampling process at training time. Specifically, we draw one third of samples nearer the camera than the depth prediction, one third in the region close to it, and one third farther away. We also provide these depth predictions as an additional input to F and regularize ρ and Λ_t to be consistent with them, which improves convergence.

²All network architectures are given in Appendix A

³We tried instead conditioning F by having a *hyper-network* directly predict its weights; this gave comparable results but proved to be much less stable during training

To avoid degenerate solutions, we apply several other regularizers on the predictions of our model. To do so, we render 2D flow and component segmentation maps \mathcal{F}_t and \mathcal{M}_t^j for each frame x_t . Inspired by classical structure-from-motion techniques, we extract keypoint tracks from the ground-truth frames using the self-supervised method [9]. We then require that the frame-to-frame displacements of the keypoints are consistent with \mathcal{F}_t . We also L1-regularize the component velocities, which avoids difficult-to-recover local optima where the motion is very large, and TV-L1 regularize [4, 25] the component masks \mathcal{M}_t^j . Further details of these regularizers are given in Appendix C.

3 Related Work

Stochastic multi-frame video prediction. Early works on video prediction did not account for the fact the the future is uncertain [36, 12, 7], hence tended to produce blurry or averaged predictions on real-world data [2, 13]. Recently there has been increasing work on *stochastic* prediction methods, which do account for this uncertainty, usually with variational inference [21]. These methods typically have one latent embedding variable per frame, with frames also conditioned on prior frames in an autoregressive fashion. [8] and [14] use ConvLSTMs for the decoder and encoder, with the prior distribution on the latents also dependent on preceding frames. [46] present an extension using deeper networks to achieve improved visual fidelity. [13] extend this further, with an ODE-inspired residual architecture to improve the dynamics model. [2] again use a variational approach, but with a more sophisticated generative process that composes output frames from transformed regions of the input frames. [24] augment the usual variational reconstruction loss with an adversarial term, to produce sharper results. Instead of variational training, [23] propose an approach based on normalizing flows [37]; this allows maximizing the exact likelihood, at the expense of an extremely computationally-heavy model. Most of these methods are evaluated exclusively on datasets with a static camera [2, 13, 8]; moreover, the majority focus on multi-frame inputs—a considerably easier setting as object velocities can be observed.

Structured video prediction. A separate line of work aims to decompose videos into a set of objects, model their dynamics, and hence predict future frames. These are broadly similar in spirit to our model, but all consider objects as 2D entities rather than 3D, which limits their applicability to real-world datasets. [48] predicts videos from a single frame, in terms of a set of moving objects defined by bounding-boxes; however they assume access to ground-truth boxes (or a pretrained detector) during both training and testing. [31] learns to auto-encode videos through a latent space that explicitly represents the locations of a set of keypoints, while also learning a dynamics model on that space. [22] construct a latent representation similar to early work on object-centric image generation [11], but with a more-sophisticated dynamics model and the ability to generate conditioned on input frames. [26] learn a 2D sprite-based representation jointly with a dynamics model over those sprites; this allows video extrapolation on simple datasets that can be adequately modelled by 2D sprites. Lastly, [47, 34] both predict frames by reasoning over optical flow (in 2D and 3D respectively), but assume access to additional information—depth images for [34], and segmentation masks for [47].

Structured video generation. Several recent methods build unconditional generative models of video, by modelling the video in terms of a set of objects. [19, 6, 45] model objects as 2D sprites, and focus on evaluating tracking and segmentation rather than generation. [16] focuses on generation, treating objects as 3D, but only considering short, synthetic videos. These methods can sample videos *a priori*, but are unable to condition on provided frames.

Related NeRFs. Our method uses a novel extension of NeRF [30] to represent 4D scenes. [33] present an alternative approach to this; however, they focus on the single-scene setting, i.e. training one model to represent a single scene given multiple views—in contrast to our setting of inferring the representation from a single image. In contrast, [49] consider predicting a NeRF from one or few images, but only to represent a static scene.

4 Experiments

Datasets. We evaluate our model on two challenging datasets of real-world videos. Waymo Open Perception [42] (WAYMO) contains 1150 videos of length 20s at 10FPS, filmed by an autonomous

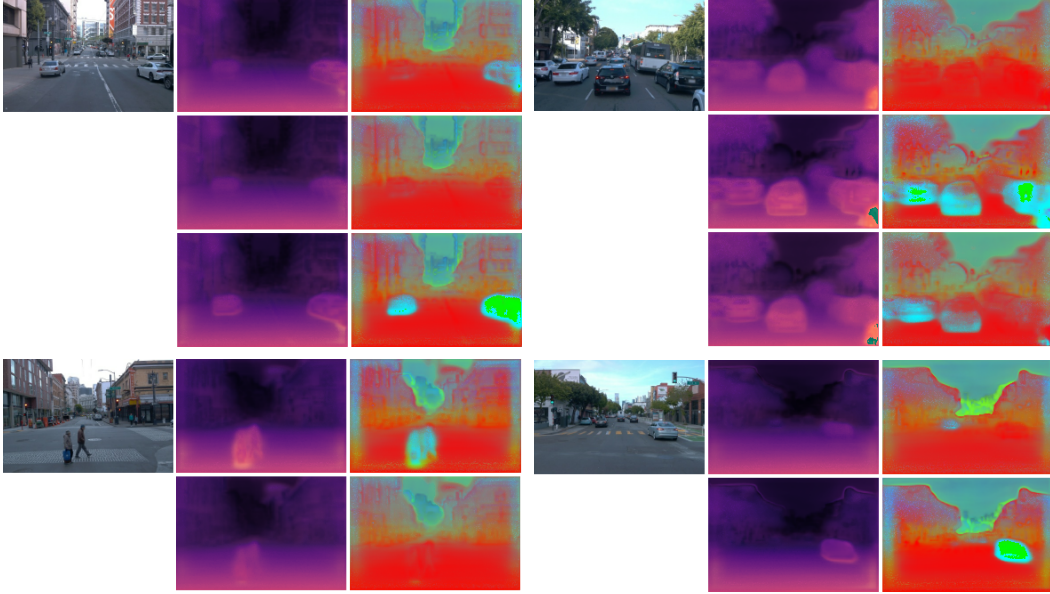


Figure 2: Depth and motion-segmentation predictions from the first frame of four clips from WAYMO. For each clip we show the input frame, the 3D structure (as a depth map; brighter is nearer), and the motion segmentation (different colors correspond to different motion components, i.e. comoving entities). The rows are 2–3 different samples from our model (i.e. different draws of z); we see the model predicts diverse motion segmentations, where different cars and pedestrians are either static or moving. Predicted depths are similar across samples—as expected since depth is much less ambiguous than motion given just one frame.

car’s sensor suite⁴. We use the main front-facing camera only, and the official train/validation/test splits. As this dataset is relatively small, for final evaluation on the test split, we train on the union of the train and val splits, keeping the hyperparameters fixed. We downsample the frames to 384×256 to use as input for our model, and use 6-frame clips. RealEstate10K [51] (RE10K) contains approximately 79000 videos of varying duration, typically a few seconds⁵. For testing, we use the first 250 videos from the validation split, as there is no test set released. The original dataset has a frame-rate of 30FPS; we subsample it to 10FPS, which makes the task more challenging as there is more movement from frame to frame. We downsample then center-crop the frames to 384×256 , and use 12-frame clips. For both datasets, we use the provided camera intrinsics (i.e. focal length and principal point). During training we sample clips randomly from within each video; we also apply data augmentation: random horizontal flipping, and random perturbations to contrast and color (see Appendix D for details). During testing we take just one clip per video, starting at the first frame. We emphasize that the chosen datasets have significant camera motion and perspective effects, in contrast to datasets often used to evaluate video prediction that have a static camera and background [40, 18, 10].

Models. We name our model *ViPLAS*, short for Video Prediction with Latent 4D Scenes. On WAYMO, we compare three variants of our model. $\text{ViPLAS}_{\text{gm}}$ uses the general camera motion model (2), allowing arbitrary motion. $\text{ViPLAS}_{\text{veh}}$ uses the more-specialized vehicle motion model, with fewer degrees of freedom in the motion parametrization. $\text{ViPLAS}_{6\text{-cpt}}$ uses six motion components, instead of four for the previous variants. Thus, the model can separate the scene into more independently-moving regions, which may be beneficial in scenes with a large number of vehicles moving at different velocities. On RE10K, we only use the general motion parametrization ($\text{ViPLAS}_{\text{gm}}$), as the videos are shot using handheld cameras and drones. We also do not experiment with more motion components, as moving objects are exceedingly rare in this dataset. We implemented our model in TensorFlow [1]; the code will be made public soon. Hyperparameters were set by incremental searches over groups of related parameters; we did not perform an exhaustive search due to computational constraints. The

⁴This dataset is licensed for research use and available at <https://waymo.com/open/>

⁵This dataset is available at <https://google.github.io/realstate10k/>, with no license specified

Table 1: Quantitative performance on video prediction for our method (ViPL4S) and SRVP [13] on two datasets. For descriptions of metrics, please see main text. Note that our method outperforms SRVP according to every metric. Small numbers give the standard deviation over three random seeds.

		FVD ↓	KVD ↓	PSNR ↑	SSIM ↑	LPIPS ↓
WAYMO	ViPL4S _{gm}	1052 ±232	188.5 ±31.6	23.16 ±0.52	0.648 ±0.035	0.266 ±0.041
	ViPL4S _{veh}	827 ±37	160.5 ±5.8	23.60 ±0.15	0.673 ±0.013	0.251 ±0.009
	ViPL4S _{6-cpt}	1015 ±120	189.4 ±21.9	22.97 ±0.09	0.653 ±0.015	0.278 ±0.009
	SRVP	2087 ±142	269.4 ±7.3	20.84 ±0.09	0.493 ±0.002	0.574 ±0.037
RE10K	ViPL4S _{gm}	647 ±24	51.0 ±1.1	18.72 ±0.32	0.536 ±0.017	0.343 ±0.016
	SRVP	1163 ±14	79.6 ±0.9	16.68 ±0.08	0.414 ±0.003	0.594 ±0.005

values used for our experiments are given in Appendix E. As a baseline, we use the state-of-the-art stochastic video prediction model *SRVP* [13]. We adapted their publicly-available implementation⁶ slightly to our setting, increasing the encoder and decoder depth, and re-tuned the hyperparameters on our datasets. Each model was trained on four Nvidia GTX 1080 Ti GPUs (or two for SRVP) on a local compute cluster, until validation-set convergence or for a maximum of five days (whichever was sooner).

Metrics. We evaluate performance using five metrics. *PSNR*, *SSIM*, and *LPIPS* [50] are standard image-similarity metrics; to evaluate stochastic video generation, we follow the common protocol [8, 24, 13] of drawing 100 samples from our model for each input, evaluating the metrics on each sample, and taking the best. These three metrics therefore measure how similar is the closest sample from a model to the ground-truth clip. Fréchet video distance (*FVD*) [44] and kernel video distance (*KVD*) [3, 44] measure how close a *distribution* of generated videos is to the ground-truth distribution; they both operate by passing sets of ground-truth and generated videos through the action-recognition network of [5], then measuring divergences of the resulting distributions of features. These two metrics therefore measure the realism and diversity of outputs from a model, without considering whether the *true* future frames are predicted for each clip. For a fair comparison with [13], we sample images at 128×128 resolution for the quantitative evaluation—the same as for their model. For all results, we report the mean and standard deviation over three runs with different random seeds.

Results. Quantitative results from our method and the baseline are given in Table 1. On both datasets, our general model ViPL4S_{gm} outperforms SRVP [13] across all metrics. In particular, higher PSNR and SSIM, and lower LPIPS, indicate that the closest samples from our model to the true frames for each clip, are significantly more similar than the closest samples from SRVP. The difference is significantly smaller for PSNR, likely because this is less sensitive to small-scale and textural details, which we found SRVP predicts poorly. FVD and KVD are substantially lower for our method, indicating that the distribution of clips generated is also closer to the ground-truth distribution than those generated by SRVP. Overall, PSNR, SSIM and LPIPS are worse for RE10K than WAYMO; this may be due to larger areas of the image being textured than WAYMO, which has extensive, smooth sky and road regions (note that FVD and KVD are not directly comparable across datasets, due to the nature of the metrics [44]).

The two additional variants of our model tested on WAYMO, ViPL4S_{veh} and ViPL4S_{6-cpt} also perform better than SRVP. However, the 6-component variant is slightly worse than the standard (4-component) variant, despite having strictly greater expressive power. We hypothesize this is due to optimization difficulties, as we observed for example that the model may reach local optima where several components are used to model different parts of the static background, when one would suffice. In contrast, the variant with a camera motion parametrization specialized to vehicles performs slightly better than that with a general motion model. While the differences are within error bars for some metrics, this still provides some support for the hypothesis that incorporating extra prior knowledge helps the generative model learn efficiently.

In Figure 2, we show examples of the 3D structure and motion segmentations predicted by our model ViPL4S_{veh} for clips from WAYMO. For each input frame, the model samples diverse but plausible

⁶The code is Apache licensed and available at <https://github.com/edouardelasalles/srvp>

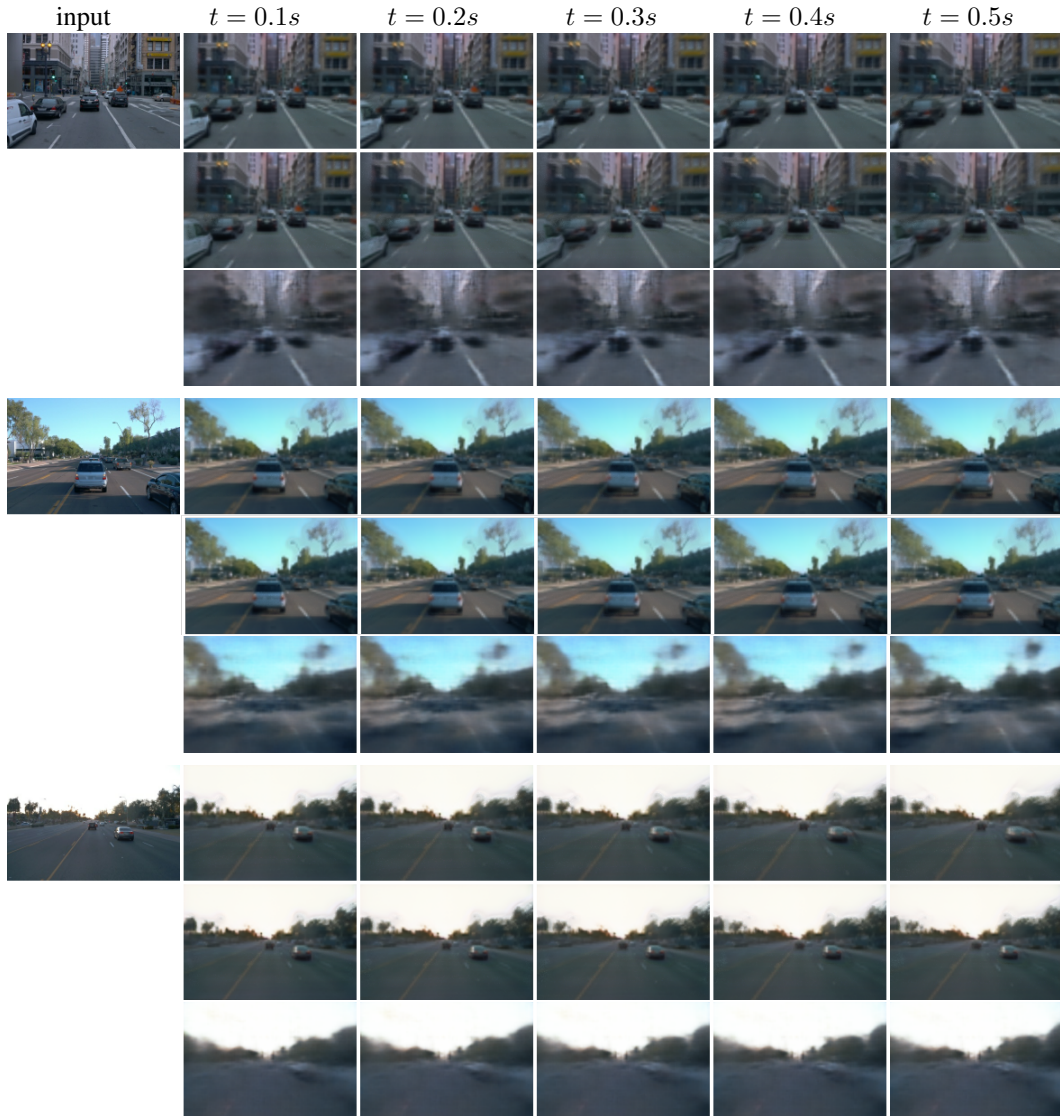


Figure 3: Videos predicted by our model and SRVP [13] given an initial frame from three clips in WAYMO. The left column is the input frame; the remaining columns shown different time steps into the future. For each input frame, we show two different samples from our model. We see that our model (first two rows for each clip) samples diverse yet plausible camera and car velocities—note the changes in relative position among vehicles and background. SRVP (third row for each clip) fails to model the motion of the camera through the scene coherently. *Best viewed as animations—click the images to link to the project page.*

motion segmentations. In particular, it has discovered without supervision that cars are sometimes (but not always) in motion, as are pedestrians. In Figure 3 we show examples of clips sampled from the same model, and from SRVP [13]. Our ability to segment moving cars results in sequences where we can observe relative motion between camera, cars and background, including significant variation between samples for the same input frame. The corresponding samples from SRVP typically do not exhibit coherent motion, in contrast to those from our model.

Finally, we show sampled clips and 3D structure for RE10K in Figure 4, for both ViPL4S and SRVP. Here we model longer (12-frame) sequences, but only show every second frame. The depth-maps are typically accurate around edges, but poor in untextured regions, due to the lack of learning signal here from the reconstruction loss. Still, the reconstructed clips are plausible; the model has successfully learnt how the camera moves in the training data (e.g. it does not pass through walls).

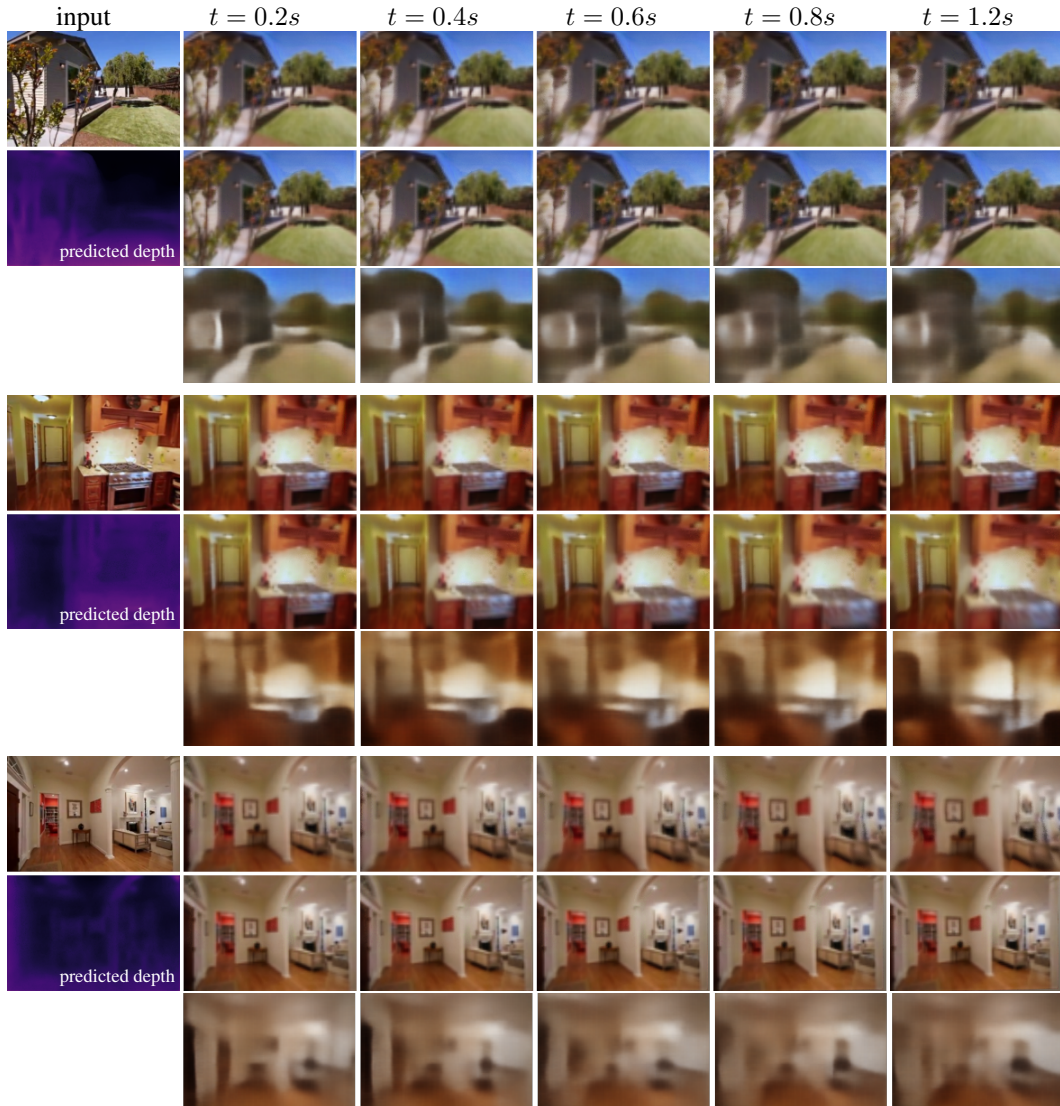


Figure 4: Videos predicted by our model and SRVP [13] given an initial frame from RE10K. We model 12-frame clips, but show only every 2nd frame. We also show the depth map predicted by ViPL4S from one sample (brighter is nearer). Our model (first two rows for each clip) has learnt a reasonable distribution of camera motion (i.e. the camera moves smoothly without passing through objects); the 3D structure represented by the depth-map is less well-defined than for WAYMO, particularly in untextured regions. SRVP (third row for each clip) fails to capture the textural details of the sequence, nor model the motion coherently. *Best viewed as animations—click the images to link to the project page.*

5 Discussion

Limitations. As the first model of its kind to address video prediction via a 4D scene representation and without supervision, our approach currently has several limitations:

- It is more computationally-expensive to sample clips at test time than the baseline [13], due to the requirement to evaluate the scene function F at many locations along every ray.
- We do not incorporate sophisticated inductive biases in the dynamics model (e.g., [31, 22, 19, 26])—we simply predict the object motion in ‘one shot’ from a densely-connected network.

- Ideally, the component assignments ω_j would be one-hot, but in practice we must relax them to allow gradient-based training. An unfortunate consequence is the introduction of local optima where points are assigned partly to one component and partly to another; this results in ‘ghosting’ artifacts where an object appears to move in two directions at once.
- It can be seen in Figure 2 that the sky is often assigned to the same motion component as moving foreground objects. The model does not receive a significant penalty for this, as the sky is both very distant and lacking textural detail, so moving at the speed of a pedestrian or even a car has negligible effect on the resulting frames.
- We currently assume that the object appearances remain constant over time, whereas in fact the *albedo* should remain so, yet illumination changes. It would therefore be valuable to incorporate recent work on separating these in the NeRF representation [41].

Conclusion. We have presented a new model *ViPLAS* that can predict video clips from a single frame. It incorporates an explicit, stable and consistent representation of the 4D scene depicted by the resulting clip. Moreover, we have seen that on two challenging real-world datasets, it can sample diverse and plausible futures, with differing object and camera motion. Finally, we showed that its quantitative performance significantly exceeds that of an existing state-of-the-art method that cannot exploit 3D structure [13].

Acknowledgments and Disclosure of Funding

This research was supported by the Scientific Service Units (SSU) of IST Austria through resources provided by Scientific Computing (SciComp).

References

- [1] Martín Abadi, Ashish Agarwal, Paul Barham, Eugene Brevdo, Zhifeng Chen, Craig Citro, Greg S. Corrado, Andy Davis, Jeffrey Dean, Matthieu Devin, Sanjay Ghemawat, Ian Goodfellow, Andrew Harp, Geoffrey Irving, Michael Isard, Yangqing Jia, Rafal Jozefowicz, Lukasz Kaiser, Manjunath Kudlur, Josh Levenberg, Dandelion Mané, Rajat Monga, Sherry Moore, Derek Murray, Chris Olah, Mike Schuster, Jonathon Shlens, Benoit Steiner, Ilya Sutskever, Kunal Talwar, Paul Tucker, Vincent Vanhoucke, Vijay Vasudevan, Fernanda Viégas, Oriol Vinyals, Pete Warden, Martin Wattenberg, Martin Wicke, Yuan Yu, and Xiaoqiang Zheng. TensorFlow: Large-scale machine learning on heterogeneous systems, 2015.
- [2] Mohammad Babaeizadeh, Chelsea Finn, Dumitru Erhan, Roy H. Campbell, and Sergey Levine. Stochastic variational video prediction. In *ICLR*, 2018.
- [3] Mikolaj Bińkowski, Dougal J. Sutherland, Michael N. Arbel, and Arthur Gretton. Demystifying MMD GANs. In *ICLR*, 2018.
- [4] Y. Boykov and M. P. Jolly. Interactive graph cuts for optimal boundary and region segmentation of objects in N-D images. In *ICCV*, 2001.
- [5] Joao Carreira and Andrew Zisserman. Quo vadis, action recognition? a new model and the kinetics dataset. In *CVPR*, 2017.
- [6] Eric Crawford and Joelle Pineau. Exploiting spatial invariance for scalable unsupervised object tracking. In *AAAI*, 2020.
- [7] Bert De Brabandere, Xu Jia, Tinne Tuytelaars, and Luc Van Gool. Dynamic filter networks. In *NIPS*, 2016.
- [8] Emily Denton and Rob Fergus. Stochastic video generation with a learned prior. In *ICML*, 2018.
- [9] Daniel DeTone, Tomasz Malisiewicz, and Andrew Rabinovich. SuperPoint: Self-supervised interest point detection and description. In *CVPR*, 2018.
- [10] Frederik Ebert, Chelsea Finn, Alex Lee, and Sergey Levine. Self-supervised visual planning with temporal skip connections. In *CoRL*, 2017.
- [11] S. M. Ali Eslami, Nicolas Heess, Theophane Weber, Yuval Tassa, David Szepesvari, Koray Kavukcuoglu, and Geoffrey E. Hinton. Attend, infer, repeat: Fast scene understanding with generative models. In *NIPS*, 2016.

- [12] Chelsea Finn, Ian Goodfellow, and Sergey Levine. Unsupervised learning for physical interaction through video prediction. In *NIPS*, 2016.
- [13] Jean-Yves Franceschi, Edouard Delasalles, Mickael Chen, Sylvain Lamprier, and Patrick Gallinari. Stochastic latent residual video prediction. In *ICML*, 2020.
- [14] Jiawei He, Andreas Lehrmann, Joseph Marino, Greg Mori, and Leonid Sigal. Probabilistic video generation using holistic attribute control. In *ECCV*, 2018.
- [15] Kaiming He, Georgia Gkioxari, Piotr Dollár, and Ross Girshick. Mask R-CNN. In *ICCV*, pages 2980–2988, 2017.
- [16] Paul Henderson and Christoph H. Lampert. Unsupervised object-centric video generation and decomposition in 3D. In *NeurIPS*, 2020.
- [17] Irina Higgins, Loic Matthey, Arka Pal, Christopher Burgess, Xavier Glorot, Matthew Botvinick, Shakir Mohamed, and Alexander Lerchner. β -VAE: Learning basic visual concepts with a constrained variational framework. In *ICLR*, 2017.
- [18] Catalin Ionescu, Dragos Papava, Vlad Olaru, and Cristian Sminchisescu. Human3.6M: Large scale datasets and predictive methods for 3D human sensing in natural environments. *IEEE Trans. on PAMI*, 2014.
- [19] Jindong Jiang, Sepehr Janghorbani, Gerard de Melo, and Sungjin Ahn. SCALOR: Generative world models with scalable object representations. In *ICLR*, 2020.
- [20] Diederik P. Kingma and Jimmy Lei Ba. Adam: A method for stochastic optimization. In *ICLR*, 2015.
- [21] Diederik P. Kingma and Max Welling. Auto-Encoding Variational Bayes. In *ICLR*, 2014.
- [22] Jannik Kossen, Karl Stelzner, Marcel Hussing, Claas Voelcker, and Kristian Kersting. Structured object-aware physics prediction for video modeling and planning. In *ICLR*, 2020.
- [23] Manoj Kumar, Mohammad Babaeizadeh, Dumitru Erhan, Chelsea Finn, Sergey Levine, Laurent Dinh, and Durk Kingma. VideoFlow: A conditional flow-based model for stochastic video generation. In *ICLR*, 2020.
- [24] Alex X. Lee, Richard Zhang, Frederik Ebert, Pieter Abbeel, Chelsea Finn, and Sergey Levine. Stochastic adversarial video prediction, 2018. arXiv:1804.01523 [cs.CV].
- [25] Hanhan Li, Ariel Gordon, Hang Zhao, Vincent Casser, and Anelia Angelova. Unsupervised monocular depth learning in dynamic scenes. In *CoRL*, 2020.
- [26] Zhixuan Lin, Yi-Fu Wu, Skand Peri, Bofeng Fu, Jindong Jiang, and Sungjin Ahn. Improving generative imagination in object-centric world models. In *ICML*, 2020.
- [27] Wei-Chiu Ma, Shenlong Wang, Rui Hu, Yuwen Xiong, and Raquel Urtasun. Deep rigid instance scene flow. In *CVPR*, 2019.
- [28] Ricardo Martin-Brualla, Noha Radwan, Mehdi S. M. Sajjadi, Jonathan T. Barron, Alexey Dosovitskiy, and Daniel Duckworth. NeRF in the wild: Neural radiance fields for unconstrained photo collections. In *CVPR*, 2021.
- [29] N. Max. Optical models for direct volume rendering. *IEEE Trans. on Visualization and Computer Graphics*, 1(2):99–108, 1995.
- [30] Ben Mildenhall, Pratul Srinivasan, Matthew Tancik, Jonathan T. Barron, Ravi Ramamoorthi, and Ren Ng. NeRF: Representing scenes as neural radiance fields for view synthesis. In *ECCV*, 2020.
- [31] Matthias Minderer, Chen Sun, Ruben Villegas, Forrester Cole, Kevin Murphy, and Honglak Lee. Unsupervised learning of object structure and dynamics from videos. In *NeurIPS*, 2019.
- [32] Ethan Perez, Florian Strub, Harm de Vries, Vincent Dumoulin, and Aaron Courville. FiLM: Visual reasoning with a general conditioning layer. In *AAAI*, 2018.
- [33] Albert Pumarola, Enric Corona, Gerard Pons-Moll, and Francesc Moreno-Noguer. D-NeRF: Neural radiance fields for dynamic scenes. In *CVPR*, 2020.
- [34] Xiaojuan Qi, Zhengzhe Liu, Qifeng Chen, and Jiaya Jia. 3D motion decomposition for RGBD future dynamic scene synthesis. In *CVPR*, 2019.

- [35] René Ranftl, Katrin Lasinger, David Hafner, Konrad Schindler, and Vladlen Koltun. Towards robust monocular depth estimation: Mixing datasets for zero-shot cross-dataset transfer. *IEEE Trans. on PAMI*, 2020.
- [36] MarcAurelio Ranzato, Arthur Szlam, Joan Bruna, Michael Mathieu, Ronan Collobert, and Sumit Chopra. Video (language) modeling: a baseline for generative models of natural videos, 2014. arXiv:1804.01523 [cs.CV].
- [37] Danilo Rezende and Shakir Mohamed. Variational inference with normalizing flows. In *ICML*, 2015.
- [38] Danilo Jimenez Rezende, Shakir Mohamed, and Daan Wierstra. Stochastic backpropagation and approximate inference in deep generative models. In *ICML*, 2014.
- [39] O. Ronneberger, P. Fischer, and T. Brox. U-Net: Convolutional networks for biomedical image segmentation. In *MICCAI*, 2015.
- [40] Christian Schuldt, Ivan Laptev, and Barbara Caputo. Recognizing human actions: A local svm approach. In *Proc. ICPR*, 2004.
- [41] Pratul P. Srinivasan, Boyang Deng, Xiuming Zhang, Matthew Tancik, Ben Mildenhall, and Jonathan T. Barron. NeRV: Neural reflectance and visibility fields for relighting and view synthesis. In *CVPR*, 2021.
- [42] Pei Sun, Henrik Kretzschmar, Xerxes Dotiwalla, Aurelien Chouard, Vijaysai Patnaik, Paul Tsui, James Guo, Yin Zhou, Yuning Chai, Benjamin Caine, Vijay Vasudevan, Wei Han, Jiquan Ngiam, Hang Zhao, Aleksei Timofeev, Scott Ettinger, Maxim Krivokon, Amy Gao, Aditya Joshi, Sheng Zhao, Shuyang Cheng, Yu Zhang, Jonathon Shlens, Zhifeng Chen, and Dragomir Anguelov. Scalability in perception for autonomous driving: Waymo open dataset. In *CVPR*, 2020.
- [43] Matthew Tancik, Pratul P. Srinivasan, Ben Mildenhall, Sara Fridovich-Keil, Nithin Raghavan, Utkarsh Singhal, Ravi Ramamoorthi, Jonathan T. Barron, and Ren Ng. Fourier features let networks learn high frequency functions in low dimensional domains. In *NeurIPS*, 2020.
- [44] Thomas Unterthiner, Sjoerd van Steenkiste, Karol Kurach, Raphaël Marinier, Marcin Michalski, and Sylvain Gelly. FVD: A new metric for video generation. In *ICLR Workshop on Deep Generative Models for Highly Structured Data*, 2019.
- [45] Rishi Veerapaneni, John D. Co-Reyes, Michael Chang, Michael Janner, Chelsea Finn, Jiajun Wu, Joshua Tenenbaum, and Sergey Levine. Entity abstraction in visual model-based reinforcement learning. In *CoRL*, 2020.
- [46] Ruben Villegas, Arkanath Pathak, Harini Kannan, Dumitru Erhan, Quoc V. Le, and Honglak Lee. High fidelity video prediction with large stochastic recurrent neural networks. In *NeurIPS*, 2019.
- [47] Yue Wu, Rongrong Gao, Jaesik Park, and Qifeng Chen. Future video synthesis with object motion prediction. In *CVPR*, 2020.
- [48] Yufei Ye, Maneesh Singh, Abhinav Gupta, and Shubham Tulsiani. Compositional video prediction. In *ICCV*, 2019.
- [49] Alex Yu, Vickie Ye, Matthew Tancik, and Angjoo Kanazawa. pixelNeRF: Neural radiance fields from one or few images. In *CVPR*, 2021.
- [50] Richard Zhang, Phillip Isola, Alexei A. Efros, Eli Shechtman, and Oliver Wang. The unreasonable effectiveness of deep features as a perceptual metric. In *CVPR*, 2018.
- [51] Tinghui Zhou, Richard Tucker, John Flynn, Graham Fyffe, and Noah Snavely. Stereo magnification: Learning view synthesis using multiplane images. *ACM Trans. Graph. (Proc. SIGGRAPH)*, 37, 2018.

A Network Architectures

Here we describe the encoder and decoder network architectures for each component of our model. Unspecified parameters are assumed to take Keras defaults.

A.1 Variational encoder enc_ϕ

```
Downsampling3D(factor=[1, 2, 2])
Conv3D(32, kernel size=[1, 7, 7], strides=[1, 2, 2], activation=relu)
GroupNormalization(groups=4)
Conv3D(48, kernel size=[1, 3, 3], activation=relu)
Conv3D(64, kernel size=[3, 1, 1], activation=relu)
MaxPool3D(size=[1, 2, 2])
GroupNormalization(groups=8)
Conv3D(48, kernel size=[1, 3, 3], activation=relu)
Conv3D(64, kernel size=[3, 1, 1], activation=relu)
MaxPool3D(size=[1, 2, 2])
GroupNormalization(groups=8)
Conv3D(48, kernel size=[1, 3, 3], activation=relu)
Conv3D(64, kernel size=[2, 1, 1], activation=relu)
MaxPool3D(size=[1, 2, 2])
Conv3D(128, kernel size=[1, 3, 3], activation=relu)
GroupNormalization(groups=8)
Flatten
Dense(512, activation=relu)
Residual(Dense(activation=relu))
Dense(128 × 2)
```

A.2 Scene function F

```
Dense(192, activation=relu)
Dense(192)
LayerNormalization
FiLM
LeakyReLU
Dense(1 + 3 + J) } × 3 with residual connections
```

A.3 Conditioning Network

A.3.1 U-net

Downsampling2D(factor=2)
Conv2D(48, kernel size=[3, 3], activation=relu)
GroupNormalization(groups=8)
MaxPool2D(size=[2, 2])
Conv2D(64, kernel size=[3, 3], activation=relu)
GroupNormalization(groups=8)
MaxPool2D(size=[2, 2])
Conv2D(96, kernel size=[3, 3], activation=relu)
GroupNormalization(groups=8)
MaxPool2D(size=[2, 2])
Conv2D(128, kernel size=[3, 3], activation=relu)
GroupNormalization(groups=8)
MaxPool2D(size=[2, 2])
Conv2D(192, kernel size=[3, 3], activation=relu)
GroupNormalization(groups=8)
MaxPool2D(size=[2, 2])
Conv2D(192, kernel size=[3, 3], activation=relu)
concatenate with latent z to give ξ'
Upsampling2D(factor=2),
concatenate with skip connection
Conv2D(192, kernel size=[3, 3], activation=relu)
GroupNormalization(groups=8)
Upsampling2D(factor=2),
concatenate with skip connection
Conv2D(128, kernel size=[3, 3], activation=relu)
GroupNormalization(groups=8)
Upsampling2D(factor=2),
concatenate with skip connection
Conv2D(96, kernel size=[3, 3], activation=relu)
GroupNormalization(groups=8)
Upsampling2D(factor=2),
concatenate with skip connection
Conv2D(64, kernel size=[3, 3], activation=relu)
GroupNormalization(groups=8)

A.3.2 ξ' to ξ

Conv2D(256, kernel size=[3, 3], activation=relu)
GroupNormalization(groups=16)
Flatten
Dense(1024, activation=relu)
LayerNormalization
Residual(Dense(activation=relu))

A.3.3 ξ to FiLM conditioning

Residual(Dense(activation=relu))
LayerNormalization
Residual(Dense(activation=relu))
LayerNormalization
Residual(Dense(activation=relu))
LayerNormalization

A.3.4 ξ to component transformation parameters

Dense(512, activation=relu)
Dense($(L - 1) \times J \times 2$, kernel initializer=zeros)

A.3.5 ξ to camera transformation parameters (ViPL4S_{gm})

Dense(512, activation=relu)
Dense($(L - 1) \times 5$, kernel initializer=zeros)

A.3.6 ξ to camera transformation parameters (ViPL4S_{veh})

Dense(512, activation=relu)
Dense($(L - 1) \times 2$, kernel initializer=zeros)

B Camera Transformation Parametrizations

As noted in the main text (Section 2), we consider two different parametrizations for the camera transformations Λ_t . The first allows arbitrary translation and rotation, while the second is specialized to cameras mounted on vehicles.

General motion. We map the embedding ξ to five values per frame, representing xyz translation, yaw (azimuth) and pitch (elevation). These values are interpreted as absolute values of the parameters (i.e. not velocities or changes from the previous frame). We apply the corresponding transformations to the camera in the order pitch, then yaw, then translation. We assume camera roll is zero, which is the case for all our datasets, and that the full transformation in the initial frame is the identity.

Vehicle motion. For this parametrization, we assume that all camera motion occurs in the xz (ground) plane. We map the embedding ξ to two values per frame, representing forward speed s_t , and azimuthal velocity α_t . The absolute azimuth a_t at frame t is then given by $\sum_{t'=1}^t \alpha_{t'} s_{t'}$; note that α_t is multiplied by the forward speed, so when the vehicle is stationary (zero speed), it is also not allowed to be rotating. The linear velocity v_t at frame t is given by $(\sin a_t, 0, -\cos a_t) \cdot s_t$, and the position by $\sum_{t'=1}^t v_{t'}$.

C Regularizers

As noted in the main text, we use several regularizers to prevent degenerate solutions. We pretrain the unsupervised single-frame depth-prediction method of [25] on our data, yielding approximate depth-maps d_t for every input frame. We also extract keypoint tracks from the input frames using the self-supervised method [9]. Then when reconstructing frame x_t during training, we render 2D flow and segmentation maps \mathcal{F}_t and \mathcal{M}_t^j . These are calculated similarly to the RGB pixels x_t , as in Eq. (2)–(4) of the main text, but replacing the colors $c(\cdot)$ with the flow (from the initial frame to frame t) and motion component indicators respectively. Given these quantities, we define the following regularizers:

- L1 regularization on the velocities of motion components, i.e. translations between successive component transformations T_t^j :

$$\frac{1}{J} \sum_j \frac{1}{L} \sum_t \left\| T_t^j(\mathbf{0}) - T_{t-1}^j(\mathbf{0}) \right\|_1 \quad (5)$$

- Edge-aware TV-L1 regularization [4, 25, 16] on the component masks \mathcal{M}_t^j , penalizing boundaries between motion components for occurring in areas where the ground-truth image x_t^* has small spatial gradients. Specifically, let K_G be a 5×5 Gaussian smoothing kernel,

and D_x, D_y be central-difference derivative kernels; for each reconstructed frame t and motion component j , we then minimize

$$\int_{\Omega} \left\{ \left| D_x * \mathcal{M}_t^j \right| \exp(-\zeta |D_x * K_G * x_t^*|) + \left| D_y * \mathcal{M}_t^j \right| \exp(-\zeta |D_y * K_G * x_t^*|) \right\} dq \quad (6)$$

where $q \in \Omega$ ranges over pixels in a frame and ζ is a hyperparameter.

- We regularize ρ to be consistent with d_t , by first grouping sample locations r_t^k according to whether they lie within, nearer, or further than a slab around d_t of thickness $d_t \times 0.025$. For points that are nearer, we regularize them to have near-zero density, by minimizing $R[p - 0.01]$ where $R[\cdot]$ is ReLU, and

$$p = 1 - \prod_j \left\{ 1 - \left(1 - \exp \left\{ -\rho \left((T_t^j)^{-1} [r_k^t] \right) \right\} \right) \omega_j \left((T_t^j)^{-1} [r_k^t] \right) \right\} \quad (7)$$

is the probability of a ray terminating in unit distance near the sample location. For points that are within the slab, we regularize them to have large density, by minimizing $R[0.975 - p] \times 6.5/W$, where W is the total number of such points and 6.5 is an empirically-determined weighting factor. Note that we normalize by W in this case but not for points nearer than the slab, as we only require one point within the slab (i.e. near the predicted depth) to have high density.

- L2 regularization on the difference between the predicted flows \mathcal{F}_t and the displacements along keypoint tracks. Specifically, for each frame t and each keypoint that appears in both the initial frame (at location k_0) and the t^{th} frame (at location k_t), we minimize $\|(k_t - k_0) - \mathcal{F}_t(k_0)\|$ where $\mathcal{F}_t(k_0)$ gives the image-space predicted flow from the initial frame to frame t , at location k_0 in the initial frame.
- L2 regularization on the difference between the true keypoint locations and reprojected locations based on d_t and Λ_t . Specifically, for each frame t and each keypoint that appears in both the initial frame (at location k_0) and the t^{th} frame (at location k_t), we calculate $\tilde{k}_t^j = \pi_t T_t^j \pi_0^{-1} k_0 \forall j$, where π_t is the projective transformation mapping a 3D point to image-space according to the camera transformation Λ_t ; then we minimize $\min_j \|k_t - \tilde{k}_t^j\|$. Thus, we require that the motion of the camera and one of the components is consistent with the observed motion of the keypoint.

D Data Augmentation

We apply the following data augmentation during training, uniformly to whole clips:

- Random horizontal flipping, with probability $\frac{1}{2}$
- Random additive perturbation of HSV color, mapping (h, s, v) to $(h + \delta h, s + \delta s, v + \delta v)$ with $\delta h \in [-0.05, 0.05]$, $\delta s \in [-0.2, 0.1]$, $\delta v \in [-0.1, 0.1]$, followed by clamping to $[0, 1]$
- Random contrast adjustment by a factor $f \in [0.8, 1.2]$, mapping component x of each pixel to $(x - \mu) \cdot f + \mu$, where μ is the mean of that channel across all pixels

E Hyperparameters

Here we list all hyperparameters for our model ViPL4S_{gm}. Note that our other model variants ViPL4S_{veh} and ViPL4S_{6-cpt} use the same hyperparameters with the exceptions described in the main text, i.e. ViPL4S_{6-cpt} sets $J = 6$.

Model	
dimensionality of z	128
component count J	4 (WAYMO) / 1 (RE10K)
image size	384×256
Loss	
pixel standard deviation	0.085
KL weight β	1
KL annealing steps	50000
L1 velocity strength	0.1
edge-aware TV-L1 strength	10
edge-aware TV-L1 ζ	10
d_t to ρ consistency strength	100
keypoint to \mathcal{F}_t consistency strength	2
keypoint to d_t consistency strength	500
Optimization	
batch size	8
learning rate	10^{-4}

The following lists those hyperparameters for the baseline SRVP [13] which we changed from their default values.

image size	128×128
batch size	120
dimensionality of y	64
dimensionality of z	64
pixel standard deviation	0.05
conditioning frames	1
sequence length	6 (WAYMO) / 12 (RE10K)
